Pergamon

*J. Mech. Phys. Solids*, Vol. 46, No. 1, pp. 85–113, 1998

0022–5096/97 $17.00+0.00

PII: S0022–5096(97)00036–7

# NONLINEAR STRESS–STRAIN CURVES FOR SOLIDS CONTAINING CLOSED CRACKS WITH FRICTION

BRIAN R. LAWN

Materials Science and Engineering Laboratory, National Institute of Standards and Technology, Gaithersburg, MD 20899, U.S.A.

DAVID B. MARSHALL

Rockwell Science Center, 1049 Camino Dos Rios, Thousand Oaks, CA 91360, U.S.A.

(*Received* 11 *February* 1997; *in revised form* 17 *May* 1997)

## ABSTRACT

Solutions for the uniaxial stress–strain response of a body containing a distribution of non-interacting nonlinear cracks are derived. First, building on energy formalisms outlined by previous workers, general solutions are derived for the body containing cracks with dissipative tractions at their surfaces, in either tension or compression loading. The special case of a body in compression loading with sliding closed cracks governed by a general friction law is then considered as a case study. The friction law contains two shear resistance terms: a "friction coefficient" term proportional to the resolved normal compression stress across the crack plane; and a "cohesion" term representing the intrinsic shear resistance of the closed crack. Inclusion of the latter term is critical to the existence of a well-defined yield point in the stress–strain curve. It is assumed that the cracks do not extend at their ends during the loading–unloading–reloading cycle; they are, however, allowed to undergo reverse sliding during the unloading. Two crack distributions are considered: all cracks aligned, leading to linear expressions for both the elastic and quasi-plastic stress–strain regions; and cracks randomly oriented, with more complex (but nonetheless tractable) expressions for the quasi-plastic regions. The resultant nonlinear stress–strain curves exhibit cyclic hysteresis, to an extent dependent on friction and crack configuration parameters. Illustrative stress–strain curves are generated for selected ranges of these controlling parameters. An outcome of the analysis is the potential link to microstructural variables, via the crack configuration parameter, offering the prospect for predictions of damage accumulation in real microstructures. The model also offers the prospect of accounting for fatigue properties, via attrition of the frictional resistance at the sliding crack surfaces. 

Keywords: A. fracture mechanisms, A. microcracking, A. microstructures, B. constitutive behavior, B. friction.

## 1. INTRODUCTION

The class of problems involving ordinarily brittle materials with nonlinear constitutive stress–strain responses has received surprisingly little attention in the mechanics literature. Such nonlinear responses are common in rocks (Jaeger and Cook, 1971; Paterson, 1978) and concretes (Shah, *et al.*, 1995), and even in some ceramics (Lawn *et al.*, 1994a; Padture and Lawn, 1995a,b), under constrained compression loading. In those cases the nonlinearity is attributable to sliding friction at pre-existent internal

crack-like defects (Ashby and Hallam, 1986; Horii and Nemat-Nasser, 1986; Nemat-Nasser and Obata, 1988; Kemeny and Cook, 1991; Myer *et al.*, 1992) or incipient microstructural "shear faults" (Lawn *et al.*, 1994a). Nonlinear responses are also observed in certain otherwise brittle solids under tension loading, e.g. ceramics containing "bridged" cracks where frictional tractions from grains (Mai and Lawn, 1987; Swanson *et al.*, 1987), reinforcing fibers or whiskers (Cox and Marshall, 1991) or metal ligaments (Evans, 1990) restrain crack separation. Experimentally, the nonlinearity is manifested as a departure from ideal elasticity above some threshold "yield" stress in the loading half-cycle, with hysteresis on unloading.

Linear problems, on the other hand, have been widely addressed, especially by those concerned with effective elastic moduli of bodies containing arrays of microscopic cracks. If the cracks do not extend or multiply the loading response remains linear, although with reduced modulus relative to an ideal uncracked solid, and again with possible hysteresis on unloading. A classic example is a compressively loaded body containing an array of identical closed cracks governed by a simple coefficient of sliding friction (Walsh, 1965; Jaeger and Cook, 1971). The load–unload stress–strain curve for this system has three branches: (i) loading branch, linear through the origin, but with reduced modulus owing to continuous frictional sliding at the crack interfaces; (ii) partial unloading branch, linear but with intrinsic modulus corresponding to that of an uncracked solid, reflecting a transient delay in sliding as the friction reverses; (iii) final unloading branch, linear back through the origin, with even lower modulus than during loading, as reverse sliding is activated. Linear solutions are also available for various crack geometries in tension and for various effective media approximations (Budiansky and O'Connell, 1976; Horii and Nemat-Nasser, 1983; Hashin, 1988), for fluid-filled cracks (Budiansky and O'Connell, 1976), and for crack arrays with interactions (Kachanov, 1992; Kachanov, 1994). Nonlinear stress–strain solutions in the loading half-cycle exist only for cases where the cracks are allowed to extend from their ends Ashby and Hallam, 1986; Horii and Nemat-Nasser, 1986; Nemat-Nasser and Obata, 1988; Kemeny and Cook, 1991; Myer *et al.*, 1992).

In the first part of this paper (Section 2) we derive generalized solutions for an isotropic body containing a random three-dimensional distribution of non-interacting, stationary, nonlinear cracks for use as a basis for damage modelling. We begin by considering the energetics for cracks governed by a nonlinear constitutive displacement–stress relation, and thence present a formulation for the stress–strain response. The stress state is conveniently taken to be uniaxial, tension or compression, but may be readily extended to multiaxial loading.

In the second part of this paper we consider a special nonlinear crack system as an illustrative case study, first a body with a single closed crack (Section 3) and then a body with multiple non-interacting closed cracks (Section 4), in uniaxial compression. The problem is similar to the one described by Walsh (1965), but with sliding governed by a more generalized friction law. Specifically, the friction law includes an additional "cohesion" term, representing the shear resistance of the closed crack interface in the absence of any superimposed normal stress (Bowden and Tabor, 1986; Nemat-Nasser and Obata, 1988), and thereby contains provision for the description of a yield point in the stress–strain curve. Again, it is assumed that the cracks do not extend or increase in density during the loading–unloading cycle, although the number of

actively sliding cracks in the existing population may be a function of load. Due attention is given to the ensuing conditions for forward and reverse crack-interface sliding during loading and unloading, allowing for cyclic hysteresis. Nonlinear stress–strain relations are then derived, and illustrative load–unload curves generated, for a range of crack densities and sizes and friction terms. A key outcome of the analysis is the explicit form of these relations, offering in those cases where the cracks are associated with the microstructure a potential link to characteristic material parameters.

## 2. GENERAL STRESS–STRAIN RELATIONS FOR BODIES CONTAINING NONLINEAR CRACKS

In this section we derive general stress–strain relations for a body containing a distribution of randomly oriented, non-interacting slit-like cracks. The body is isotropic and linear elastic everywhere but at the crack surface, where irreversible tractions operate. These tractions are assumed to be governed by a nonlinear constitutive relation between applied stresses and crack-opening displacements. The primary source of nonlinearity of interest here is that arising from sliding frictional forces acting between closed crack surfaces in compressive loading. However, other potential sources of nonlinearity, e.g. from bridging ligaments that restrain crack opening in tensile loading, may equally well be considered. For simplicity, we will address the case of uniaxial loading. Extension to more complex, biaxial or triaxial stress states is straightforward (Kachanov, 1992; Kachanov, 1994). Our approach is analogous to that laid out by previous workers (Walsh, 1965; Budiansky and O'Connell, 1976), except that we modify the formulation in such a way as to allow for nonlinearity.

The starting point for the analysis is an expression for the complementary energy density of the cracked body as the sum of two terms: the complementary energy density for the body without cracks, plus the crack energy density $W$ (Appendix A):

$$\int_0^\sigma \varepsilon \, \mathrm{d}\sigma = \sigma^2/2E_0 + W, \tag{1}$$

where $\varepsilon$ is the average strain in the body, $\sigma$ is the applied stress and $E_0$ is Young's modulus of the uncracked body. If the cracks are non-interacting, $W$ is the sum over the energies $w_i$ of all cracks contained within the volume $V$ of the body:

$$W = (1/V) \sum_{i=1}^{NV} w_i, \tag{2}$$

where $N$ is the crack number density. Differentiation of (1) yields a general strain–stress relation:

$$\varepsilon = \sigma/E_0 + \mathrm{d}W/\mathrm{d}\sigma. \tag{3}$$

Equation (3) conveniently expresses the strain as the sum of the strain in the uncracked body and the additional nonlinear strain from the cracks.

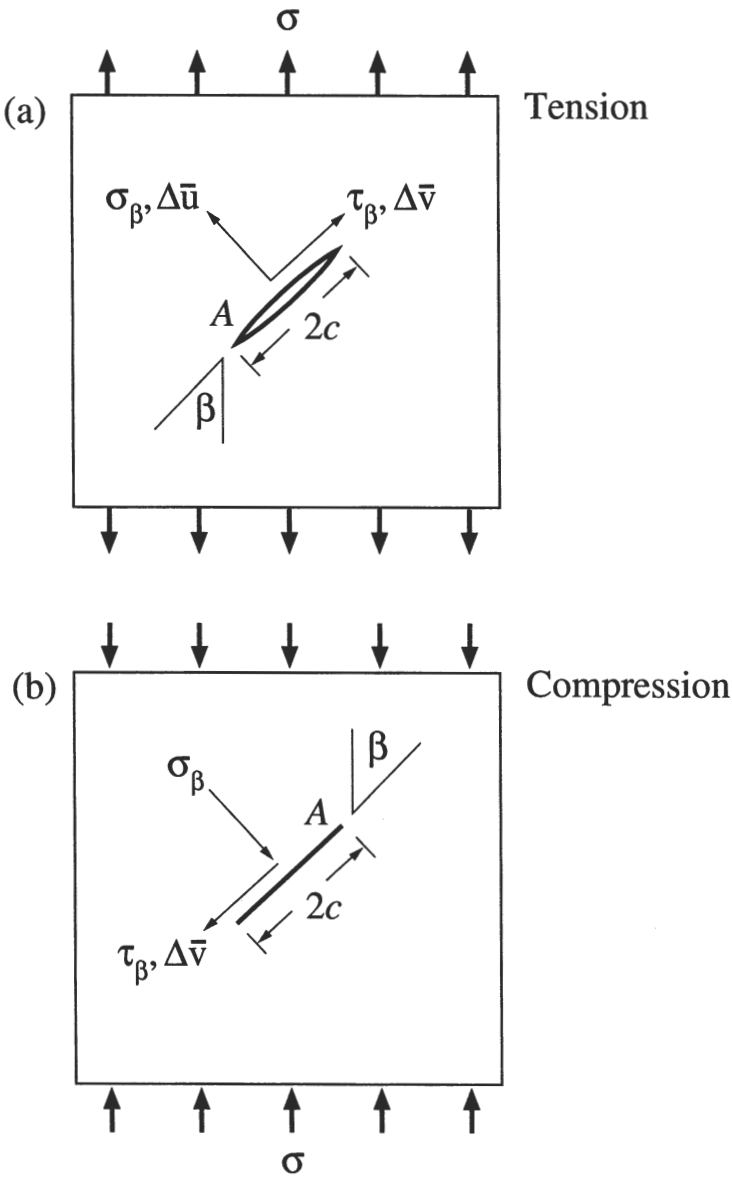


Fig. 1. Body containing crack, area $A$, characteristic length $c$ ($A = \Omega c^2$), orientation $\beta$ to applied stress $\sigma$: (a) tension, (b) compression. Resolved normal and shear stresses $\sigma_\beta$ and $\tau_\beta$, and corresponding displacements $\Delta\bar{u}(\sigma_\beta)$ and $\Delta\bar{v}(\sigma_\beta)$, indicated.

Now consider the crack energy $w$ for an elastic body containing a single internal crack of area $A$ and orientation $\beta$ relative to the applied stress $\sigma$, either tension [Fig. 1(a)], or compression [Fig. 1(b)]. Resolved normal and tangential stresses $\sigma_\beta$ and $\tau_\beta$ on the crack plane are

$$\sigma_\beta = \sigma \sin^2 \beta, \tag{4a}$$

$$\tau_\beta = \sigma \sin \beta \cos \beta, \tag{4b}$$

with corresponding displacement changes averaged over the crack area

$$\Delta\bar{u}(\sigma) = \bar{u}(\sigma) - \bar{u}(0), \tag{5a}$$

$$\Delta\bar{v}(\sigma) = \bar{v}(\sigma) - \bar{v}(0). \tag{5b}$$

In problems involving cracks in reverse loading with irreversible tractions at the crack surfaces, or where cracks are subject to internal residual stresses, nonzero values of $\bar{u}(0)$ and $\bar{v}(0)$ are encountered. The crack energy may be written (Appendix A)

$$w(\sigma, \beta) = 2A \left[ \int_0^{\sigma_\beta} \Delta\bar{u}(\sigma_\beta)\, \mathrm{d}\sigma_\beta + \int_0^{\tau_\beta} \Delta\bar{v}(\tau_\beta)\, \mathrm{d}\tau_\beta \right]$$

$$= 2A \int_0^{\sigma} [\Delta\bar{u}(\sigma, \beta) \sin^2 \beta + \Delta\bar{v}(\sigma, \beta) \sin \beta \cos \beta]\, \mathrm{d}\sigma. \tag{6}$$

Strictly, (6) is restricted to cracks with sliding displacements $\Delta\bar{v}$ parallel to the resolved shear stress $\tau_\beta$. this condition is satisfied for any crack with an elliptical front, including the limiting cases of penny and straight-front plane cracks, provided one of the elliptical axes is aligned along the direction of resolved shear stress (Appendix B). For non-aligned elliptical cracks a tensor form of (6) is needed.

Now suppose the body contains a density $N$ of non-interacting randomly oriented cracks. If $N$ is sufficiently large, the sum in (2) may be replaced by an integral over all orientations $\beta$ (Walsh, 1965; Budiansky and O'Connell, 1976):

$$W(\sigma) = N \int_0^{\pi/2} w(\sigma, \beta) \cos \beta\, \mathrm{d}\beta. \tag{7}$$

Where the cracks are of uniform shape and size, (6) and (7) may be combined to give

$$W(\sigma) = 2NA \int_0^{\pi/2} \int_0^{\sigma} \sin \beta \cos \beta [\Delta\bar{u}(\sigma, \beta) \sin \beta + \Delta\bar{v}(\sigma, \beta) \cos \beta]\, \mathrm{d}\sigma\, \mathrm{d}\beta. \tag{8}$$

Where cracks are not active over the entire angular range (as in the case for cracks with friction, Section 3), angular limits for $\beta$ in (8) need to be appropriately restricted.

The combination of (3) and (8) provides a general expression for the stress–strain curve, in terms of the crack-surface displacements $\Delta\bar{u}(\sigma, \beta)$ and $\Delta\bar{v}(\sigma, \beta)$, i.e. in terms of the constitutive behavior of the individual cracks. These two equations provide the basic starting point for the case study of cracks with frictional sliding considered in the following section.

Before concluding this section, two special cases may be noted, as follows. (i) If the angular limits for active cracks, $\beta_1$ and $\beta_2$, are independent of $\sigma$ (linear constitutive law), then (8) may be readily differentiated with respect to $\sigma$, as required in (3):

$$\mathrm{d}W/\mathrm{d}\sigma = 2NA \int_{\beta_1}^{\beta_2} \sin \beta \cos \beta [\Delta\bar{u}(\sigma, \beta) \sin \beta + \Delta\bar{v}(\sigma, \beta) \cos \beta]\, \mathrm{d}\beta, \tag{9}$$

leaving a single integral over a fixed range of $\beta$. (ii) If, further, the displacement functions $\Delta\bar{u}(\sigma, \beta)$ and $\Delta\bar{v}(\sigma, \beta)$ are both proportional to $\sigma$, (3) and (9) reduce to a linear stress–strain curve. Cases considered previously (Walsh, 1965; Budiansky and O'Connell, 1976; Horii and Nemat-Nasser, 1983; Hashin, 1988; Kachanov, 1992; Kachanov, 1994) are of this form. However, if either of these two conditions is not satisfied, the stress–strain curve is necessarily nonlinear and must be computed from the general form of (3) and (8).

## 3. STRESS–STRAIN CURVES FOR BODIES IN COMPRESSION LOADING CONTAINING CLOSED CRACKS WITH FRICTIONAL SLIDING: SINGLE-CRACK SOLUTIONS

In this section we consider the special case of a brittle solid containing a single closed crack ["shear fault" (Lawn *et al.*, 1994a)], free of internal residual stresses and with generalized sliding friction between the crack surfaces (Jaeger and Cook, 1971), in uniaxial applied compression $\sigma$. The formulation of Section 2 is applicable, with the restriction that, since the cracks are closed, normal displacements across the crack plane are precluded ($\Delta\bar{u} = 0$). Also, since we shall now be concerned exclusively with compression loading, we adopt a sign convention that takes compressive stresses and corresponding displacements as positive.

In the following section we extend the solutions to a body containing specified distributions of cracks.

### 3.1. *Constitutive friction law*

Consider a body containing a crack at orientation $\beta$ [Fig. 1(b)]. Sliding of the crack surfaces is driven by the resolved shear stress $\tau_\beta$ [equation 4(b)] on the crack plane. Let this sliding be resisted by a frictional stress $\tau_f = \tau_c + \mu\sigma_\beta$, where $\tau_c$ is a "cohesion stress", $\mu$ is a friction coefficient and $\sigma_\beta$ is the resolved normal stress [Equation 4(a)] (Horii and Nemat-Nasser, 1986; Nemat-Nasser and Obata, 1988):

$$\tau_f = \tau_c + \mu\sigma \sin^2 \beta. \tag{10}$$

This relationship has been confirmed extensively in direct measurements of friction in rocks and soils (Jaeger and Cook, 1971). Many studies (Walsh, 1965) use a simplified form of (10), with $\tau_c = 0$. We will show later that inclusion of the $\tau_c$ term is crucial to certain features of the stress–strain behavior, notably the existence of a yield stress (Nemat-Nasser and Obata, 1988).

### 3.2. *Crack sliding displacements*

The average sliding displacements of the closed crack surfaces are proportional to the net shear stresses acting on the crack. The general form is (Walsh, 1965; Budiansky and O'Connell, 1976)

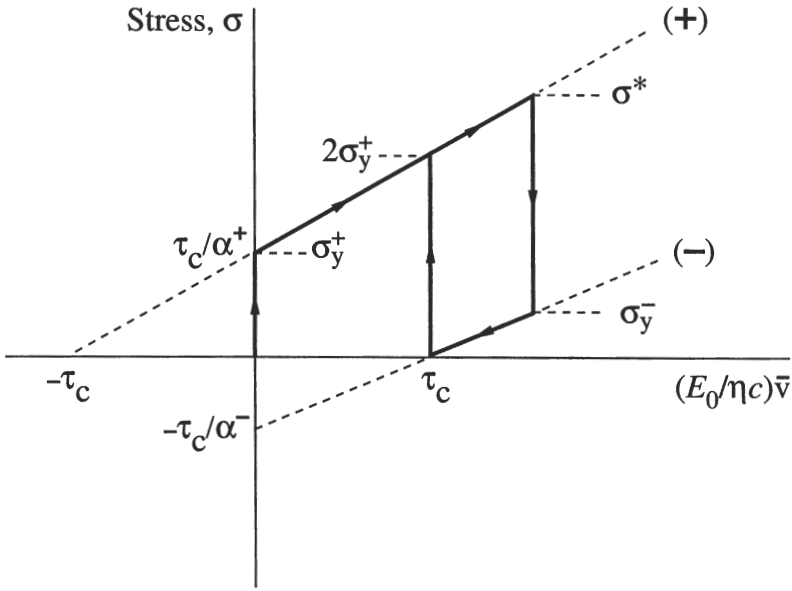


Fig. 2. Constitutive stress–displacement relation for body in compression containing single closed shear crack. Inclined lines represent sliding branches, forward (+) and reverse (−). Vertical lines represent passive non-sliding branches. Solid line segments indicate hysteretic load–unload–reload cycle.

$$\bar{v} = \begin{cases} (\eta c/E_0)(\tau_\beta - \tau_f) & (\textit{loading}), \quad (11a) \\ (\eta c/E_0)(\tau_\beta + \tau_f) & (\textit{unloading}), \quad (11b) \end{cases}$$

where $c$ is a characteristic crack dimension, related to crack area by $A = \Omega c^2$, with $\Omega$ a dimensionless constant and $\eta$ a dimensionless crack geometry constant (Appendix B): for penny cracks, $\Omega = \pi$ and $\eta = 8(1+\nu)/3\pi$. Note that it is $\bar{v}$ and not $\Delta\bar{v}$ that appears in (11); since friction is involved, provision must be made for nonzero $\bar{v}(0)$ in $\Delta\bar{v} = \bar{v}(\sigma) - \bar{v}(0)$. (Equation (11) is subject to the same restriction mentioned in the preceding subsection, that the displacements must be in the same direction as the resolved shear stresses.) With (4b) and (10), (11) may be written in terms of the applied stress $\sigma$:

$$(E_0/\eta c)\bar{v} = \begin{cases} \alpha^+(\beta)\sigma - \tau_c & (\textit{loading}), \quad (12a) \\ \alpha^-(\beta)\sigma + \tau_c & (\textit{unloading}), \quad (12b) \end{cases}$$

where we define the quantities

$$\alpha^+(\beta) = \sin\beta\cos\beta - \mu\sin^2\beta, \quad (13a)$$

$$\alpha^-(\beta) = \sin\beta\cos\beta + \mu\sin^2\beta. \quad (13b)$$

The constitutive relations in (12) are represented in Fig. 2 as a plot of applied stress $\sigma$ against displacement term $(E_0/\eta c)\bar{v}$ for a load–unload–reload cycle. Two sliding branches (inclined solid lines) are shown: forward (+) branch [equation (12a)], with displacement-axis intercept $-\tau_c$ and stress-axis intercept $\tau_c/\alpha^+$; reverse (−) branch

[equation (12b)], with displacement-axis intercept $\tau_c$ and stress-axis intercept $-\tau_c/\alpha^-$. We identify the following stages (arrows) in the hysteretic loading cycle:

(i) *Loading*. During initial loading, the crack faces do not slide until the applied shear stress equals the frictional resistance, corresponding to intersection of the vertical loading line $\bar{v} = 0$ with the upper, forward sliding branch in (12a), defining a "forward yield stress"

$$\begin{aligned}\sigma_y^+ &= \tau_c/\alpha^+(\beta) \\ &= \tau_c/(\sin\beta\cos\beta - \mu\sin^2\beta).\end{aligned} \tag{14}$$

With continued loading above $\sigma = \sigma_y^+$, forward sliding proceeds along the upper branch in Fig. 2 until the peak stress $\sigma = \sigma^*$ is reached.

(ii) *Unloading*. On unloading, the friction terms reverse sign. Initially, the crack faces remain stationary along the vertical unloading line $\bar{v} = \bar{v}(\sigma^*)$ in (12a), until this unloading line intersects the lower, reverse sliding branch $\bar{v} = \bar{v}(\sigma_y^-)$ in (12b), defining a "reverse yield stress"

$$\begin{aligned}\sigma_y^- &= [\alpha^+(\beta)\sigma^* - 2\tau_c]/\alpha^-(\beta) \\ &= [\sigma^*(\sin\beta\cos\beta - \mu\sin^2\beta) - 2\tau_c]/(\sin\beta\cos\beta + \mu\sin^2\beta).\end{aligned} \tag{15}$$

With continued unloading below $\sigma = \sigma_y^-$, reverse sliding proceeds along the lower branch in Fig. 2, leaving a residual displacement $\bar{v}(0) = \eta c\tau_c/E_0$ at $\sigma = 0$ in (12b). Note that if $\tau_c = 0$ [as taken in previous analyses (Walsh, 1965)], then $\bar{v}(0) = 0$ (the hysteretic cycle closes). Note also that no reverse sliding will occur at all if $\sigma_y^- \leqslant 0$, corresponding to $\sigma^* \leqslant 2\tau_c/\alpha^+(\beta)$ [i.e. peak stress less than twice the forward yield stress in (14)].

(iii) *Reloading*. During reloading, the crack faces remain stationary, at $\bar{v} = \eta c\tau_c/E_0$, until the forward sliding branch is again intersected, at $\sigma = \sigma_y^+$, after which this branch is followed up to $\sigma^*$. Further cycling between the same zero and peak loads then repeats the hysteretic unload–reload loop.

This hysteretic formulation lays the groundwork for a consideration of fatigue, by progressive attrition of $\mu$ and $\tau_c$, manifested in Fig. 2 as cyclic shifts in the hysteretic loop (Padture and Lawn, 1995b).

### 3.3. *Crack energy and stress–strain curve*

For a body containing a crack at orientation $\beta$ in uniaxial compression $\sigma$ [Fig. 1(b)], insertion of $\Delta\bar{u} = 0$ into (6) reduces the crack energy to

$$w(\sigma, \beta) = 2A\sin\beta\cos\beta\int_0^\sigma \Delta\bar{v}(\sigma)\,\mathrm{d}\sigma. \tag{16}$$

This integral is evaluated by inserting (12) and (13), in conjunction with (14) and (15), for the various stages of loading, unloading and reloading. The pertinent energies at any given applied stress $\sigma$ are represented by the shaded areas in the schematic

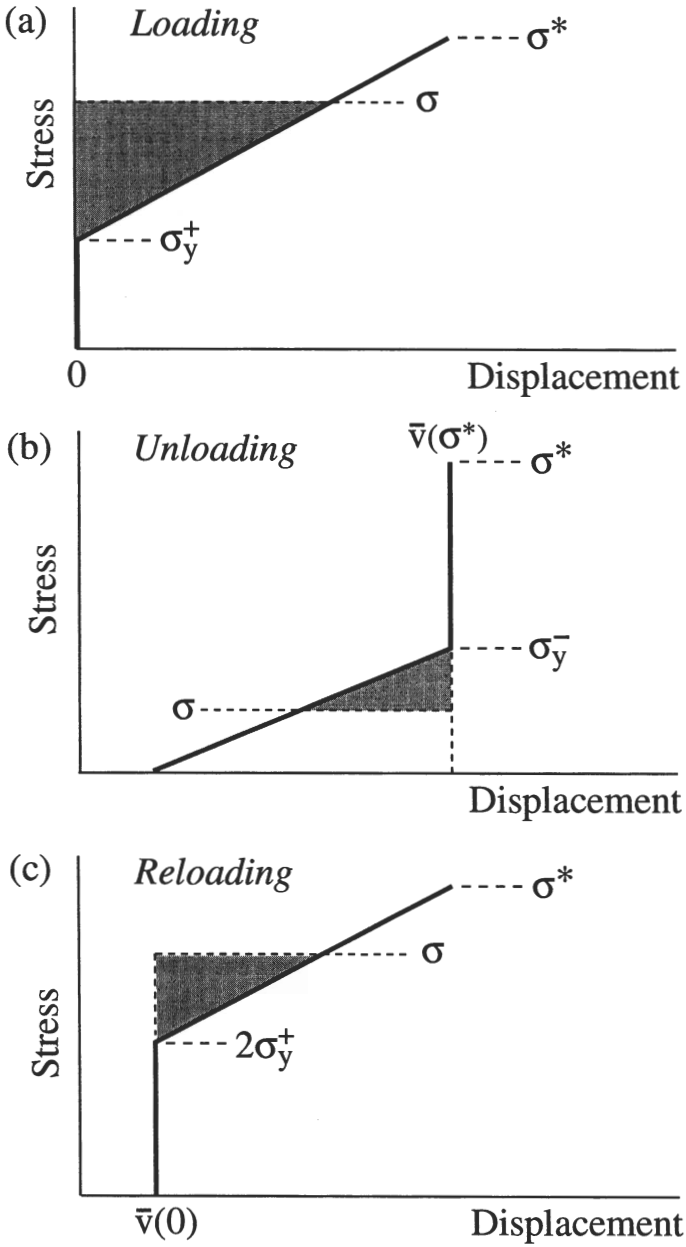


Fig. 3. Stress–displacement diagrams for body with single closed shear crack. Shaded areas represent crack energies associated with crack–surface sliding: (a) loading, (b) unloading (c) reloading.

plots of $\sigma(\bar{v})$ in Fig. 3. Note that there are zero contributions to the energy in the initially passive stages where the crack faces remain stationary: in loading within $0 \leqslant \sigma \leqslant \sigma_y^+$, unloading within $\sigma_y^- \leqslant \sigma \leqslant \sigma^*$, and reloading within $0 \leqslant \sigma \leqslant 2\sigma_y^+$. Note

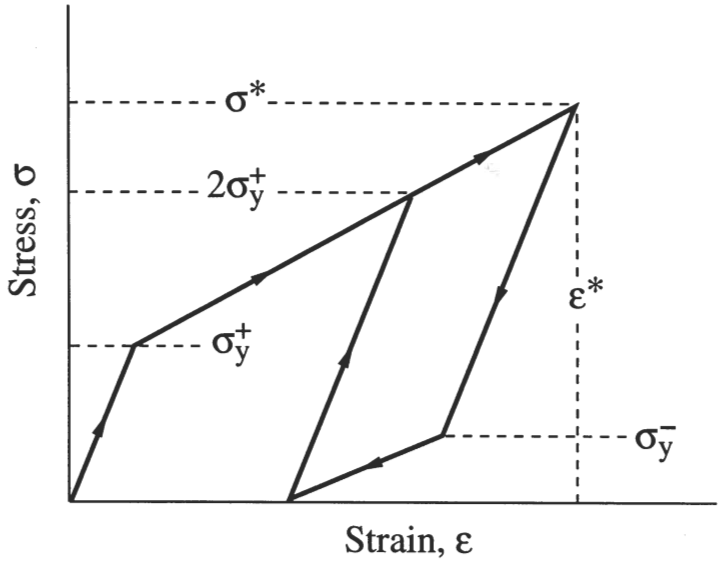


Fig. 4. Stress–strain curve for body with single closed shear crack, showing load–unload–reload cycle. Note linear segments.

also that the displacement changes used to calculate the energies, and thence the strains, are measured relative to the displacements at the beginning of sliding in each of the loading, unloading and reloading segments. Integration then gives:

$$w(\sigma,\beta)=\begin{cases}(\Omega\eta c^3/E_0)g^+(\beta)[\sigma-\sigma_y^+(\beta)]^2 & (\textit{loading},\ \sigma_y^+\leqslant\sigma\leqslant\sigma^*), \quad (17a)\\ (\Omega\eta c^3/E_0)g^-(\beta)[\sigma_y^-(\beta)-\sigma]^2 & (\textit{unloading},\ 0\leqslant\sigma\leqslant\sigma_y^-), \quad (17b)\\ (\Omega\eta c^3/E_0)g^+(\beta)[\sigma-2\sigma_y^+(\beta)]^2 & (\textit{reloading},\ 2\sigma_y^+\leqslant\sigma\leqslant\sigma^*), \quad (17c)\end{cases}$$

where again we write crack area $A$ in terms of a characteristic linear dimension $c$, $A=\Omega c^2$, and we define the quantities

$$\begin{aligned}g^+(\beta)&=\alpha^+(\beta)\sin\beta\cos\beta\\&=\sin\beta\cos\beta(\sin\beta\cos\beta-\mu\sin^2\beta),\end{aligned}\quad (18a)$$

$$\begin{aligned}g^-(\beta)&=\alpha^-(\beta)\sin\beta\cos\beta\\&=\sin\beta\cos\beta(\sin\beta\cos\beta+\mu\sin^2\beta).\end{aligned}\quad (18b)$$

It is instructive to construct the stress–strain curve $\sigma(\varepsilon)$ for this single-crack system, as in Fig. 4. During the stages of loading, unloading and reloading where the cracks remain closed and passive, branch slopes are governed by the intrinsic modulus $E_0$ of the uncracked body. Forward and reverse sliding occurs along the upper and lower sliding branches, with consequent reductions in effective modulus. On these sliding

branches, the slopes of the functions $\sigma(\varepsilon)$ are determined by substituting (17) into (3), with $W = w/V$ in (2):

$$(\mathrm{d}\sigma/\mathrm{d}\varepsilon) = \begin{cases} E_0/[1+2\Omega\eta c^3 g^+(\beta)/V] & (\textit{loading, reloading}), \quad (19a) \\ E_0/[1+2\Omega\eta c^3 g^-(\beta)/V] & (\textit{unloading}), \quad (19b) \end{cases}$$

which are independent of $\sigma$, and hence are constants. The hysteric cycle comprises linear segments in Fig. 4. Note again that a residual strain remains after unloading through the first complete cycle, and that subsequent reload/unload curves form a repeatable closed hysteresis loop (provided the friction parameters $\mu$ and $\tau_c$ do not degrade in successive cycles).

## 4. STRESS–STRAIN CURVES FOR BODIES IN COMPRESSION LOADING CONTAINING CLOSED CRACKS WITH FRICTIONAL SLIDING: MULTIPLE-CRACK SOLUTIONS

Now let us extend the analysis to a brittle solid containing a distribution of many cracks governed by the friction relation described in the previous section. To do this, we integrate the energy expressions for single cracks to determine the energies for the multiple crack system, from which the stress–strain curves may be calculated. Here, we consider two distributions: first, all cracks commonly aligned; second, cracks randomly oriented.

Before carrying out the energy and stress–strain analyses, consider the allowable crack orientation range for sliding under any given set of loading conditions.

### 4.1. *Angular limits for sliding activity*

In a body with many crack orientations, sliding activity is confined within limited ranges of $\beta$, in accordance with the conditions for forward and reverse sliding defined by the functions $\sigma_y^+(\beta)$ and $\sigma_y^-(\beta)$ in (14) and (15). These functions are plotted schematically in Fig. 5(a). The loading function $\sigma_y^+(\beta)$ has a minimum, and unloading function $\sigma_y^-(\beta)$ a maximum, at

$$\beta_{\min}^+ = \tfrac{1}{2}\arctan(1/\mu), \quad (20a)$$

$$\beta_{\max}^- = \arctan\{1/[(1+\mu^2+\mu\sigma^*/\tau_c)^{1/2}-\mu]\}, \quad (20b)$$

defining yield points $\sigma_y^+(\beta_{\min}^+)$ and $\sigma_y^-(\beta_{\max}^-)$. The active angular ranges at any given applied stress $\sigma$ are then determined as intersections between the horizontal heavy dashed line representing this stress and the appropriate $\sigma_y^+(\beta)$ and $\sigma_y^-(\beta)$ curves. The range $\beta_1^+$ to $\beta_2^+$ for forward sliding expands with increasing stress above $\sigma = \sigma_y^+(\beta_{\min}^+)$, to a maximum at $\sigma = \sigma^*$. Similarly, the range $\beta_1^-$ to $\beta_2^-$ for reverse sliding expands with decreasing applied stress below $\sigma = \sigma_y^-(\beta_{\max}^-)$, to a maximum at $\sigma = 0$. With the exception of the special case $\tau_c = 0$, the maximum range for reverse sliding is smaller than the maximum range for forward sliding. Note that in no case is the angular range of activity complete through the loading–unloading cycle.

For reloading, recall from Section 3.2 that (14) prevails, but with $\tau_c$ replaced by

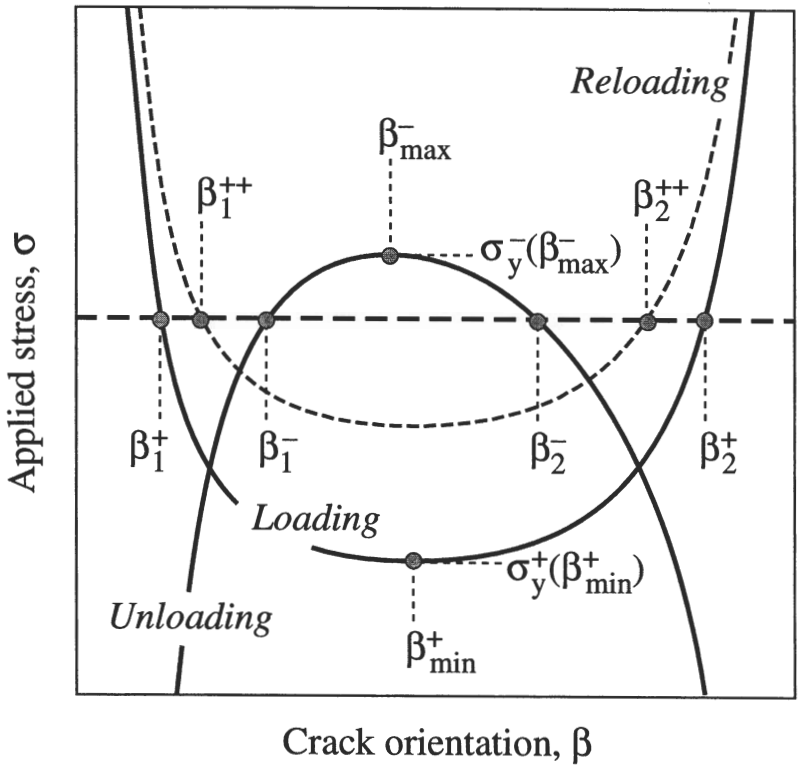


Fig. 5. Plots of loading $\sigma_y^+(\beta)$ and unloading $\sigma_y^-(\beta)$ functions in (14) and (15) (heavy curves). (a) Schematic plot, illustrating angular limits for crack-surface sliding at any specified applied stress $\sigma$ (heavy horizontal dashed line). (b) Analytical plot, for indicated values of $\tau_c/\sigma^*$, at $\mu = 0$. (c) Same as (b), but for $\mu = 0.5$.

$2\tau_c$. Hence, (20a) remains valid, and the appropriate $\sigma_y^+(\beta)$ curve is simply displaced upward on the stress axis by a factor of two, as indicated by the dashed curve in Fig. 5(a) (the unloading curves are unchanged). Accordingly, the active range $\beta_1^{++}$ to $\beta_2^{++}$ for reloading will be somewhat lower than for loading. At the same time, the maximum angular range for reloading (at $\sigma = \sigma^*$) is the same as the maximum range for reverse sliding (at $\sigma = 0$), resulting in a closed unloading–reloading hysteresis loop.

Also shown in Fig. 5 are plots of (14) and (15) for selected values of $\mu$ and $\tau_c$ (all stresses normalized to $\sigma^*$). For $\mu = 0$ [Fig. 5(b)] the extreme in these curves occur universally at $\beta = \beta^+_{min} = \beta^-_{max} = 45°$, regardless of $\tau_c$. The forward yield stress $\sigma_y^+(\beta^+_{min})$ increases, and the reverse yield stress $\sigma_y^-(\beta^-_{max})$ decreases, with increasing $\tau_c$. For $\mu = 0.5$ [Fig. 5(c)], the angular extrema shift to lower $\beta$. At the same time, $\sigma_y^+(\beta^+_{min})$ increases and $\sigma_y^-(\beta^-_{max})$ decreases still further. The net effect of increasing either of the friction parameters $\mu$ and $\tau_c$ is to diminish the angular range of crack sliding at any given stress level.

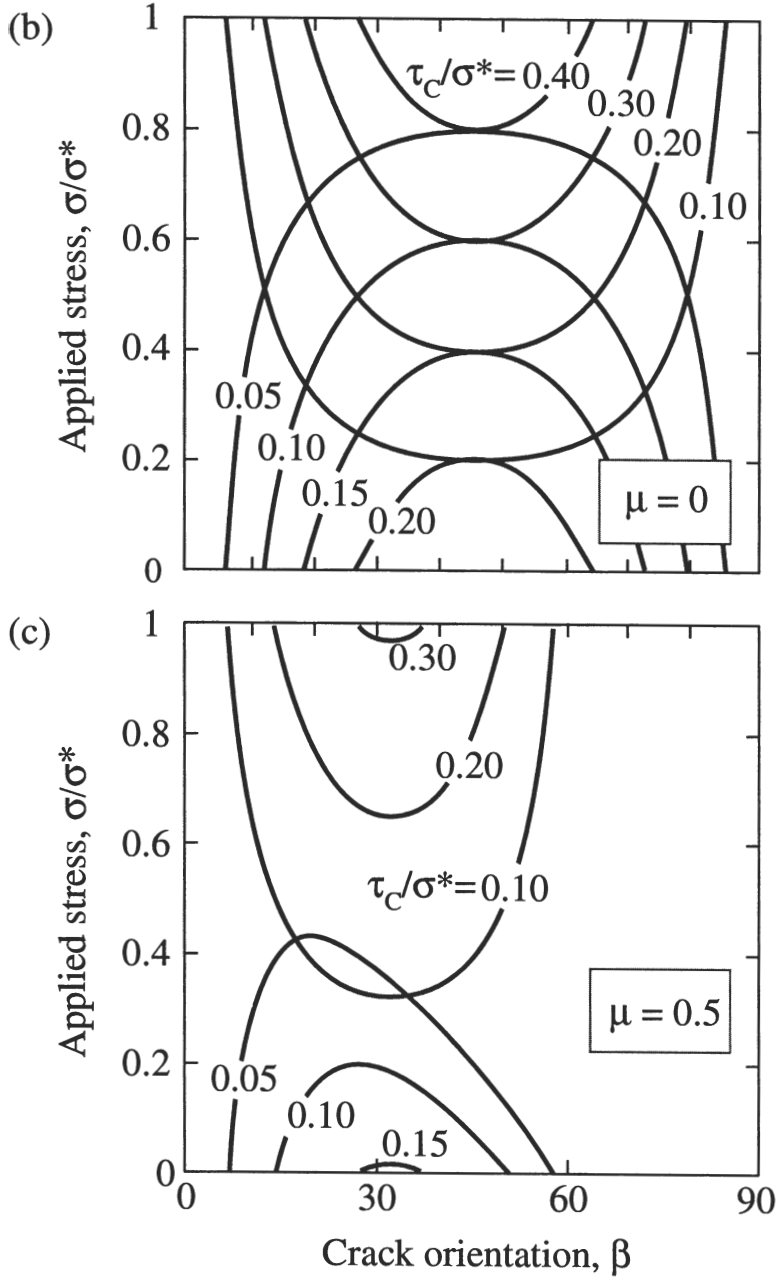


Fig. 5—*Continued.*

Generally, the limiting relations $\sigma = \sigma_y^+(\beta)$ and $\sigma = \sigma_y^-(\beta)$ in (14) and (15) must be solved numerically for $\beta_1$ and $\beta_2$, but two special cases give explicit solutions:

(i) *Zero cohesion stress*, $\tau_c = 0$, the case considered by Walsh (Walsh, 1965). We obtain

$$\beta_1^+ = 0, \quad \beta_2^+ = \arctan(1/\mu), \tag{21a}$$

$$\beta_1^- = 0, \quad \beta_2^- = \arctan[(\sigma^* - \sigma)/\mu(\sigma^* + \sigma)]. \tag{21b}$$

In this case, the loading angular range $\beta_1^+$ to $\beta_2^+$ is independent of $\sigma$. This stress independence, together with the proportional displacement–stress relation at $\tau_c = 0$ in (12), accounts for the linear loading stress–strain curve through the origin found by Walsh. The fact that the range $\beta_1^+$ to $\beta_2^+$ diminishes with increasing $\mu$ also accounts for the reduced modulus relative to the uncracked body. Note, however, that the corresponding unloading angular range $\beta_1^-$ to $\beta_2^-$ is not independent of $\sigma$, so the unloading stress–strain curve is necessarily nonlinear. Upon unloading to $\sigma = 0$, the range $\beta_1^-$ to $\beta_2^-$ in (21b) is identical to the range $\beta_1^+$ to $\beta_2^+$ in (21a)—i.e. all cracks which undergo forward sliding during loading ultimately restore at the completion of the full loading cycle to their initial state. In this case reloading simply retraces the loading curve.

(ii) *Zero friction coefficient*, $\mu = 0$. In this case, we obtain

$$\beta_1^+ = \tfrac{1}{2}\arcsin(2\tau_c/\sigma), \quad \beta_2^+ = \pi/2 - \beta_1^+, \tag{22a}$$

$$\beta_1^- = \tfrac{1}{2}\arcsin[4\tau_c/(\sigma^* - \sigma)], \quad \beta_2^- = \pi/2 - \beta_1^-, \tag{22b}$$

where the angular ranges are dependent on $\sigma$, guaranteeing a nonlinear stress–strain curve. It follows that any combination of nonzero $\tau_c$ and $\mu$ will always result in nonlinear curves. Note that the range $\beta_1^-$ to $\beta_2^-$ at complete unloading, $\sigma = 0$ in (22b), is always less than the range $\beta_1^+$ to $\beta_2^+$ at peak loading, $\sigma = \sigma^*$ in (22a), so hysteresis with residual displacements is general. In reloading, $\tau_c$ is again replaced by $2\tau_c$ in (22a).

### 4.2 *Energy and stress–strain curve: body with aligned cracks*

Now consider a body containing a density $N$ of non-interacting cracks of uniform size $c$, all aligned at some fixed orientation $\beta$. Then the energy density $W$ in (2) is simply equal to $Nw$, with $w$ from (17):

$$W(\sigma) = \begin{cases} (\rho/E_0)g^+(\beta)[\sigma - \sigma_y^+(\beta)]^2 & (\textit{loading}, \sigma_y^+ \leqslant \sigma \leqslant \sigma^*), \quad (23a) \\ (\rho/E_0)g^-(\beta)[\sigma_y^-(\beta) - \sigma]^2 & (\textit{unloading}, 0 \leqslant \sigma \leqslant \sigma_y^-), \quad (23b) \\ (\rho/E_0)g^+(\beta)[\sigma - 2\sigma_y^+(\beta)]^2 & (\textit{reloading}, 2\sigma_y^+ \leqslant \sigma \leqslant \sigma^*), \quad (23c) \end{cases}$$

where we define a dimensionless parameter containing all the configurational information (size, shape, density) on the cracks,

$$\rho = \Omega\eta N c^3. \tag{24}$$

For penny cracks and Poisson's ratio $\nu = 0.25$, $\rho = 2Nc^3$.

The assumption of fixed $\beta$ in (23) leads to explicit expressions for the stress–strain curves from (3). Moreover, by defining normalized stress $\sigma/\sigma^*$ and strains $\varepsilon E_0/\sigma^*$, these expressions take on universal forms. Then only three parameters are needed to describe the stress–strain curve completely: $\tau_c/\sigma^*$, the normalized cohesion stress; $\mu$, the friction coefficient; and $\rho$ the crack configuration coefficient. All segments of the stress–strain curve for the cracked body remain linear (cf. Fig. 4), with slopes as follows: for the passive loading–unloading–reloading branches, unity (as for the reference uncracked body); for the sliding branches, reduced values [cf. (19)].

$$\mathrm{d}(\sigma/\sigma^*)/\mathrm{d}(\varepsilon E_0/\sigma^*) = \begin{cases} 1/[1+2\rho g^+(\beta)], & (\textit{loading, reloading}), \quad (25a) \\ 1/[1+2\rho g^-(\beta)] & (\textit{unloading}). \quad (25b) \end{cases}$$

Stress–strain curves for the special crack orientation $\beta = \beta^+_{\min}$, i.e. the configuration of maximum degree of sliding, are plotted in Figs 6–8, for selected values of $\tau_c/\sigma^*$, $\mu$ and $\rho$. Various degrees of nonlinearity and hysteresis are evident (cf. Fig. 4 for notation):

(i) *Effect of cohesion stress.* Figure 6 shows curves for $\tau_c/\sigma^* = 0$, 0.1, 0.2 and 0.3, at fixed $\mu = 0.25$ and $\rho = 2$. In these plots the principal influence of $\tau_c$ is in the critical stresses $\sigma_y^+ = \sigma_y^+(\beta^+_{\min})$ and $\sigma_y^- = \sigma_y^-(\beta^+_{\min})$. At $\tau_c/\sigma^* = 0$, the loading curve is linear through the origin but with diminished modulus $E < E_0$, since all cracks within the active (load-invariant) angular range (Section 3.2) undergo immediate forward sliding at $\sigma = \sigma_y^+ = 0$. The cracks initially unload along a branch with modulus $E_0$ to $\sigma_y^-$, corresponding to the onset of reverse sliding, and thereafter along a branch with even more diminished modulus, ultimately returning to the origin. The system therefore absorbs energy in each cycle, but leaves zero residual strain. At $\tau_c/\sigma^* = 0.1$, initial loading occurs with modulus $E_0$ to a yield point $\sigma_y^+$, and thereafter with reduced slope to $\sigma^*$. Unloading again occurs along two branches, but with a lower critical reverse sliding stress $\sigma_y^-$ than at $\tau_c/\sigma^* = 0$. The hysteresis is accentuated, and the residual strain is no longer zero. At $\tau_c/\sigma^* = 0.2$, $\sigma_y^+$ is yet higher, but now $\sigma_y^- < 0$, so that while hysteresis remains pronounced, reverse sliding is suppressed. At $\tau_c/\sigma^* = 0.3$, $\sigma_y^+$ lies just below $\sigma^*$, and the hysteresis is substantially diminished.

(ii) *Effect of friction coefficient.* Figure 7 shows curves for $\mu = 0$, 0.5 and 1, at fixed $\tau_c/\sigma^* = 0.1$ and $\rho = 2$. Here, the effect of $\mu$ is felt both in the critical stresses $\sigma_y^+$ and $\sigma_y^-$ and in the slopes of the nonlinear branches. The limiting case $\mu = 0$ is that of pure cohesion-type friction. In contrast with the case $\tau_c = 0$ in Fig. 6, a yield point $\sigma_y^+$ in the loading half-cycle (as well as $\sigma_y^-$ in the loading half-cycle) is apparent, since a threshold stress must now be exceeded in order for forward sliding to occur. Hysteresis and residual strain are manifest. At $\mu = 0.5$, $\sigma_y^+$ increases and $\sigma_y^-$ decreases, and the hysteretic loop is broader. At $\mu = 1$, $\sigma_y^- < 0$, so the unloading is completely elastic, and hysteresis is diminished.

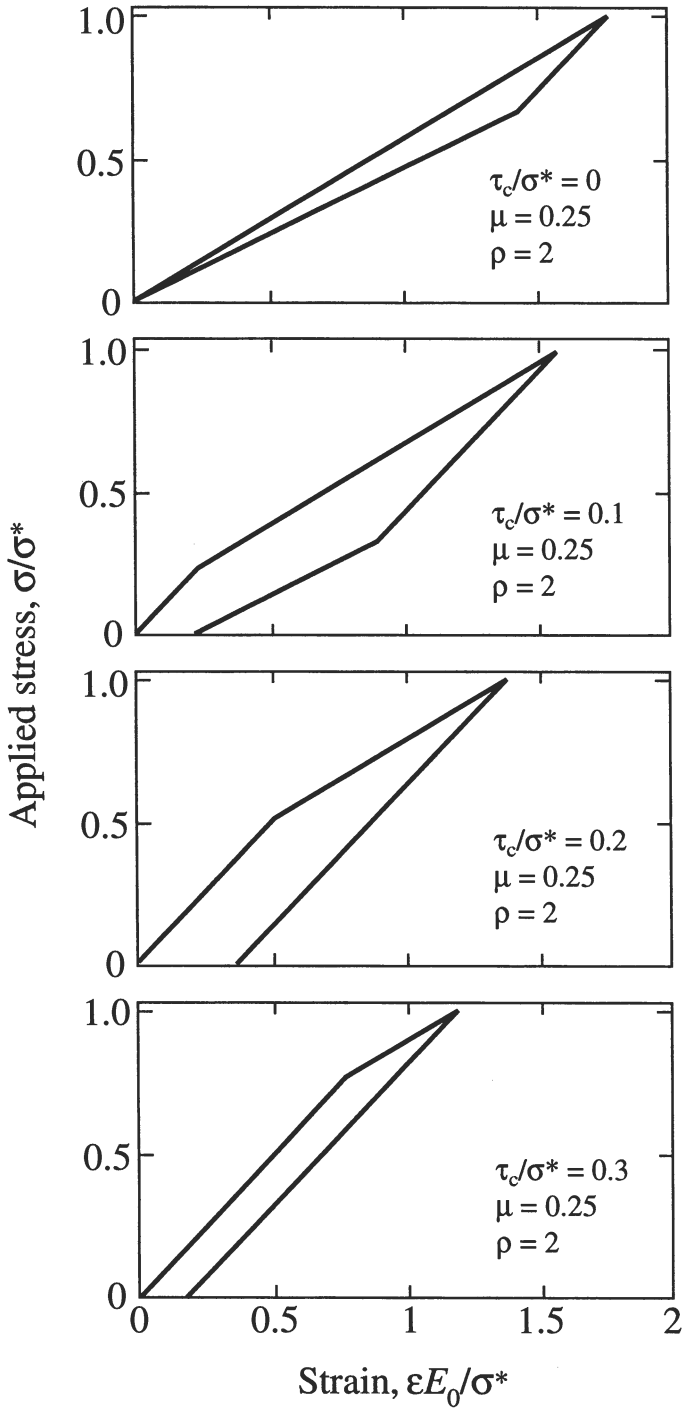


Fig. 6. Stress–strain curves for aligned cracks, evaluated from (3) and (23). Showing effect of cohesion stress: $\tau_c/\sigma^* =$ (a) 0, (b) 0.1, (c) 0.2 and (d) 0.3, at fixed $\mu = 0.25$ and $\rho = 2$.

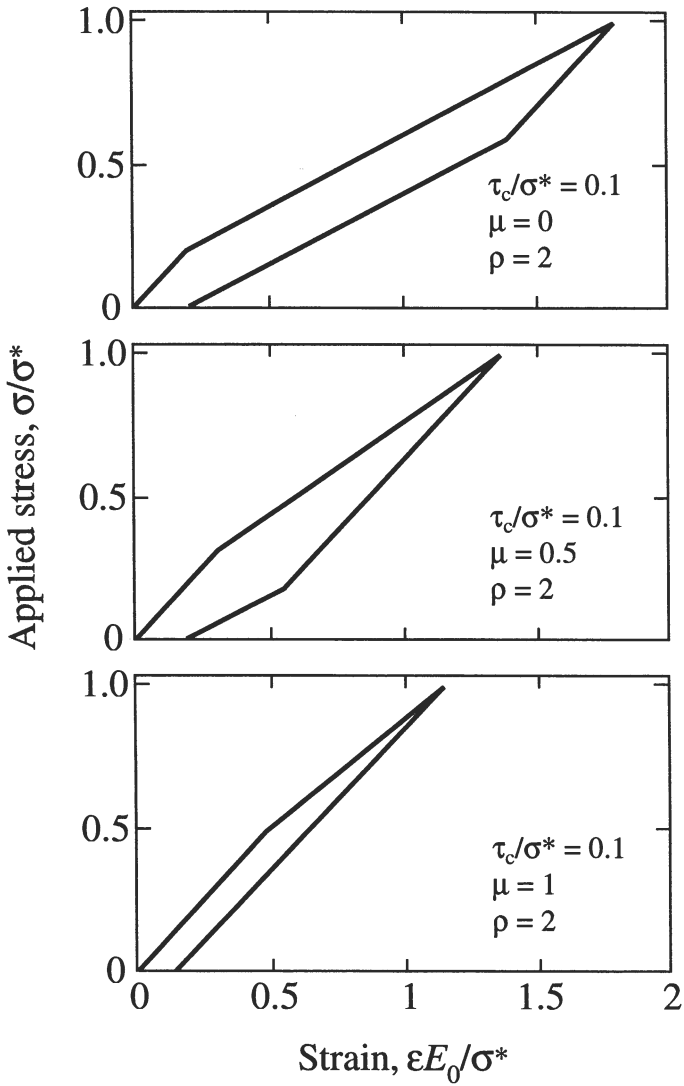


Fig. 7. Stress–strain curves for aligned cracks, evaluated from (3) and (23). Showing effect of coefficient of friction: $\mu$ = (a) 0, (b) 0.5 and (c) 1, at fixed $\tau_c/\sigma^* = 0.1$ and $\rho = 2$.

(iii) *Effect of crack density*. Figure 8 shows curves for $\rho = 0$, 1 and 2, at fixed $\tau_c/\sigma^* = 0.1$ and $\mu = 0.25$. Now it is only the slopes of the nonlinear branches that are affected, with $\sigma_y^+$ and $\sigma_y^-$ invariant. The case $\rho = 0$ is trivial, corresponding to an ideally elastic response. Increasing $\rho$ through 1 to 2 progressively decreases the slopes of the sliding branches, with attendant increasing hysteresis as the number of active sources increases.

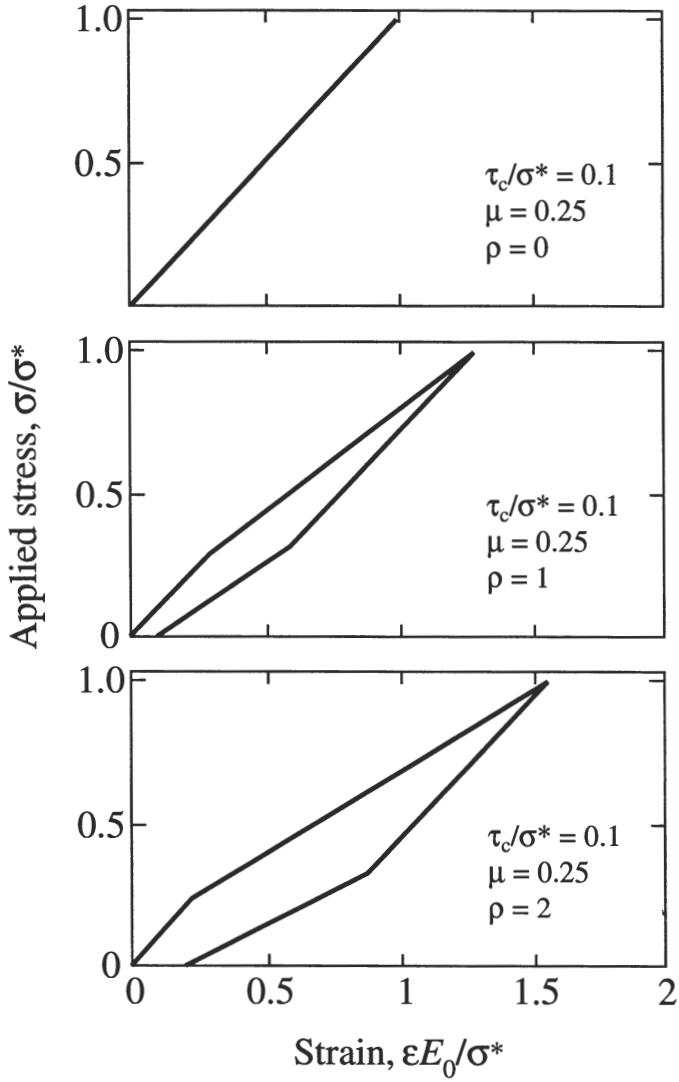


Fig. 8. Stress–strain curves for aligned cracks, evaluated from (3) and (23). Showing effect of crack density: $\rho = 0$, 1 and 2, at fixed $\tau_c/\sigma^* = 0.1$ and $\mu = 0.25$.

### 4.3. *Energy and stress–strain curve: body with randomly oriented cracks*

For the same body containing a density $N$ of non-interacting cracks of uniform size $c$, but now with the cracks randomly oriented, the energies in (7) and (17) must be integrated over all angles $\beta$ within which sliding occurs [Fig. 5(a)]:

$$W(\sigma) = \begin{cases} (\rho/E_0) \displaystyle\int_{\beta_1^+}^{\beta_2^+} g^+(\beta) \cos\beta[\sigma - \sigma_y^+(\beta)]^2 \, d\beta \\ \qquad\qquad (\textit{loading}, \sigma_y^+(\beta_{\min}^+) \leqslant \sigma \leqslant \sigma^*], & (26a) \\ (\rho/E_0) \displaystyle\int_{\beta_1^-}^{\beta_2^-} g^-(\beta) \cos\beta[\sigma_y^-(\beta) - \sigma]^2 \, d\beta \\ \qquad\qquad (\textit{unloading}, 0 \leqslant \sigma \leqslant \sigma_y^-(\beta_{\max}^-)], & (26b) \\ (\rho/E_0) \displaystyle\int_{\beta_1^{+\,+}}^{\beta_2^{+\,+}} g^+(\beta) \cos\beta[\sigma - 2\sigma_y^+(\beta)]^2 \, d\beta \\ \qquad\qquad [\textit{reloading}, 2\sigma_y^+(\beta_{\min}^+) \leqslant \sigma \leqslant \sigma^*], & (26c) \end{cases}$$

with the angular ranges determined in Section 4.1.

As in the previous subsection, it is convenient to introduce stress and strain normalizations $\sigma/\sigma^*$ and $\varepsilon E_0/\sigma^*$. Substituting (26) into (3), we obtain the dimensionless stress–strain relations:

$$\varepsilon E_0/\sigma^* = \begin{cases} \sigma/\sigma^* + \rho \, d\left\{\displaystyle\int_{\beta_1^+}^{\beta_2^+} g^+(\beta) \cos\beta[\sigma/\sigma^* - \sigma_y^+(\beta)/\sigma^*]^2 \, d\beta\right\} \Big/ d(\sigma/\sigma^*) \\ \qquad\qquad [\textit{loading}, \sigma_y^+(\beta_{\min}^+) \leqslant \sigma \leqslant \sigma^*], & (27a) \\ \sigma/\sigma^* + \rho \, d\left\{\displaystyle\int_{\beta_1^-}^{\beta_2^-} g^-(\beta) \cos\beta[\sigma_y^-(\beta)/\sigma^* - \sigma/\sigma^*]^2 \, d\beta\right\} \Big/ d(\sigma/\sigma^*) \\ \qquad\qquad [\textit{unloading}, 0 \leqslant \sigma \leqslant \sigma_y^-(\beta_{\max}^-)], & (27b) \\ \sigma/\sigma^* + \rho \, d\left\{\displaystyle\int_{\beta_1^{+\,+}}^{\beta_2^{+\,+}} g^+(\beta) \cos\beta[\sigma/\sigma^* - 2\sigma_y^+(\beta)/\sigma^*]^2 \, d\beta\right\} \Big/ d(\sigma/\sigma^*) \\ \qquad\qquad [\textit{reloading}, 2\sigma_y^+(\beta_{\min}^+) \leqslant \sigma \leqslant \sigma^*]. & (27c) \end{cases}$$

Since the limits $\beta_1$ and $\beta_2$ are themselves functions of $\sigma/\sigma^*$, $\tau_c/\sigma^*$ and $\mu$ (Section 4.1), the functions in (27) are again expressible entirely in terms of just three parameters, $\tau_c/\sigma^*$, $\mu$ and $\rho$ (Section 4.2).

Figure 9 shows a stress–strain curve computed from (27) using $\tau_c/\sigma^* = 0.1$, $\mu = 0.25$ and $\rho = 2$, for comparison with the corresponding plot for aligned cracks (dashed lines). The degree of quasi-plasticity is not so pronounced for the randomly oriented cracks, since only the most favorably aligned cracks will begin sliding at first yield.

## 5. DISCUSSION

In this study we have described a model for a body containing a distribution of closed cracks of uniform size in uniaxial loading. We have presented a general formalism for either tension or compression loading, with provision for frictional tractions at the crack interface. Special attention has been given to shear cracks in

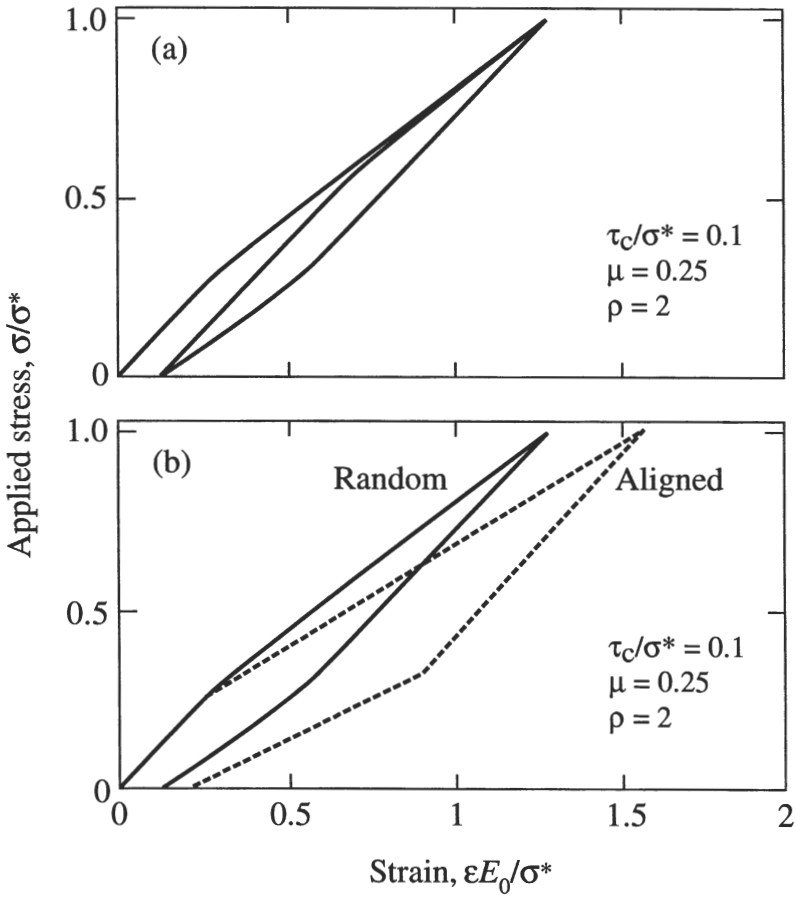


Fig. 9. Stress–strain curves for randomly oriented cracks evaluated from (3) and (26), for $\tau_c/\sigma^* = 0.1$, $\mu = 0.25$ and $\rho = 2$: (a) complete load–unload–reload cycle; (b) load–unload cycle, with corresponding result for cracks aligned at $\beta = \beta^+_{\min}$ (dashed lines).

compression loading with a crack-surface friction law of general form. The end result is a stress–strain response that is generally nonlinear, with well-defined yield stress and hysteresis in the loading–unloading–reloading cycle, as befits the real behavior of a wide range of quasi-plastic (quasi-brittle) solids. This formalism, expressible in terms of friction and crack configuration (and ultimately material microstructure—see below) parameters, may serve as a constitutive basis for analysis of damage accumulation in this interesting class of solids.

An element of the present analysis that warrants further comment is the provision for the existence of a well-defined macroscopic yield stress in compression loading, by virtue of inclusion of the cohesion term $\tau_c$ in the friction relation (10) (Sections 3 and 4). "Yield" above some initially elastic region is a distinctive feature of the stress–strain response in traditionally nonlinear materials like rocks (Jaeger and Cook, 1971) and concretes (Shah *et al.*, 1995), especially in compression testing. More recently,

quasi-plasticity has been demonstrated in tough ceramics above critical loads in Hertzian contact (Guiberteau *et al.*, 1993; Cai *et al.*, 1994a; Lawn *et al.*, 1994b), where a largely triaxial compression contact field suppresses classical cone fracture (Frank and Lawn, 1967) in these ordinarily brittle materials. This cohesion term could arise from any one of several mechanisms, whose character might alter in successive cycles: direct cohesive forces between the crack walls (chemical or van der Waals bonding); roughness of the crack walls (e.g. cleavage steps, grain boundary fractures), causing mechanical interlocking; or frictional debris trapped between the crack walls, causing residual compression stresses at the crack interface.

In quantifying this quasi-plasticity it has been found expedient to write the loading stress–strain relation in the sliding region in the empirical form (Fischer-Cripps and Lawn, 1996)

$$\sigma = Y + \alpha(\varepsilon E_0 - Y) \quad (\sigma > Y), \tag{28}$$

where $Y$ defines the yield stress, such that $\alpha = 1$ represents the limit of full elasticity and $\alpha = 0$ full plasticity. Equation (28) has the same form as the results in Section 4.2 for aligned cracks. For cracks aligned at $\beta^+_{\min}$, comparison with (14), (20a) and (25) gives

$$Y = \sigma_y^+(\beta^+_{\min}) = 2\tau_c h(\mu), \tag{29a}$$

$$\alpha = 1/[1 + \rho k(\mu)/2], \tag{29b}$$

with the friction-dependent functions

$$h(\mu) = 1/[(1+\mu^2)^{1/2} - \mu], \tag{30a}$$

$$k(\mu) = [1 - \mu/(1+\mu^2)^{1/2}]. \tag{30b}$$

Note that $Y = 0$ at $\tau_c = 0$ in (29a), confirming the necessity for $\tau_c$ to be nonzero in order for a yield stress to exist. Note also that $h(0) = 1 = k(0)$ in (30). Finally, note that for a specified peak stress $\sigma^*$ there exists an upper limit to frictional resistance beyond which crack sliding cannot occur at all during the loading cycle, defined by the condition $Y > \sigma^*$, or $2\tau_c/\sigma^* > (1+\mu^2)^{1/2} - \mu$, in (29a) and (30a). The locus of $\tau_c/\sigma^*$ and $\mu$ values that define this limiting condition is plotted in Fig. 10.

For the case of randomly oriented cracks, the stress–strain curve has a continuously varying slope beyond the yield point. However, since this variation is generally small (e.g. Fig. 9), we may closely approximate that portion of the stress–strain curve by a linear segment, similar to that for aligned cracks but with a greater slope. This linear segment may be represented by (28), but with an increased slope term $\alpha$ in (29b), corresponding to an "effective" crack density parameter $\rho'$. [Note this does not affect the yield point in (29a).] Table 1 lists best-fit ratios $\rho'/\rho$ for various values of $\tau_c/\sigma^*$ and $\mu$. Note that the values of this ratio become quite small for large friction terms.

At the fundamental microstructural level, the cracks envisioned in Fig. 1 (and especially in Section 3 and 4) originate as incipient defects within the material. In rocks and concretes, these defects are usually associated with pores, weak-phase inclusions, or pre-present cracks (Walsh, 1965; Jaeger and Cook, 1971; Paterson, 1978; Batzle *et al.*, 1980; Kranz, 1983; Zhang *et al.*, 1990; Kemeny and Cook, 1991;

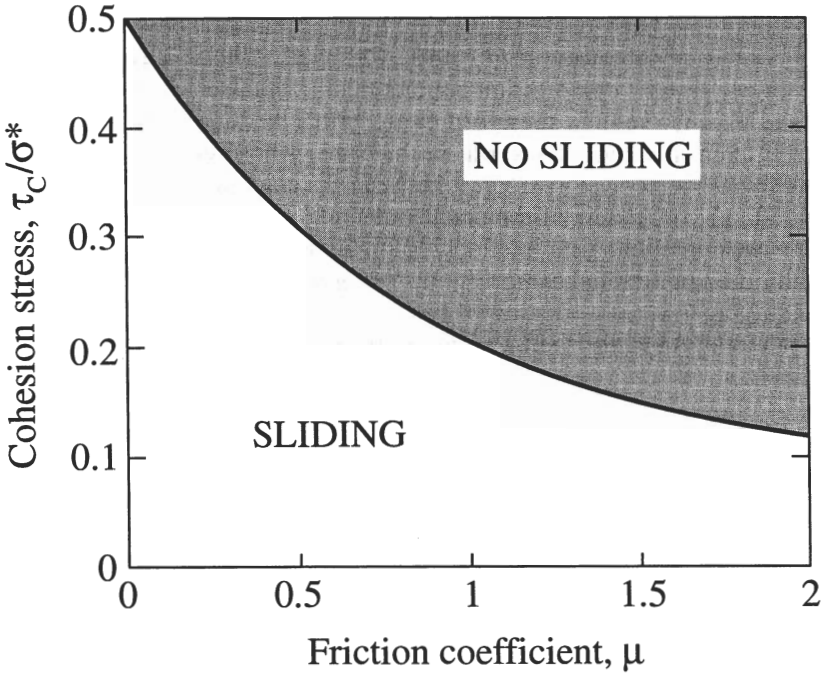


Fig. 10. Locus of $\tau_c/\sigma^*$ and $\mu$ values delineating domains of sliding and no sliding at crack surfaces.

Table 1. *Values of ratio $\rho'/\rho$ for selected friction terms*

| $\mu$ / $\tau_c/\sigma^*$ | 0 | 0.25 | 0.5 | 1 |
|---|---|---|---|---|
| 0 | 0.53 | 0.53 | 0.51 | 0.43 |
| 0.1 | 0.50 | 0.48 | 0.44 | 0.32 |
| 0.2 | 0.45 | 0.41 | 0.33 | 0.09 |
| 0.3 | 0.39 | 0.30 | 0.10 | — |

Meredith *et al.*, 1991; Wong *et al.*, 1992; Shah *et al.*, 1995). In dense ceramics, the defects are associated with weak interfaces in the microstructure, so-called "shear faults" (since they are shear-activated, exclusively in compression loading) (Lawn *et al.*, 1994b; Fischer-Cripps and Lawn, 1996). These shear faults may be twins [e.g. alumina (Guiberteau *et al.*, 1993, 1994; Wei and Lawn, 1996), silicon nitride (Xu *et al.*, 1995)], or weak grain or interphase boundaries [platelet or needle structures, e.g. in-situ toughened silicon carbide (Padture and Lawn, 1994; Padture and Lawn, 1995a, b), silicon nitride (Xu *et al.*, 1995), glass-ceramics (Cai *et al.*, 1994a, b), and particle-reinforced alumina composites (An *et al.*, 1996)].

It is through the crack configuration parameter $\rho = \Omega\eta Nc^3$ defined in (24), with its

embodiment of crack size ($c$), shape ($\Omega\eta$) and density ($N$), that we may connect the analysis most directly with the microstructure. As to shape, we have shown that $\Omega\eta = 2$ (Poisson's ratio 0.25) for the simplest case of penny cracks (Section 3.2). For the other factors, consider as an illustrative example a microstructure consisting of disk-like platelet inclusions with weak inclusion/matrix interfaces [as in several tough ceramics (Cai *et al.*, 1994a, b; Padture and Lawn, 1994, 1995a,b; An *et al.*, 1996)]; and suppose that each platelet slides along one of the large weak interfaces, i.e. one planar penny crack per platelet. The volume occupied by any one such platelet is $\pi c^2 d = \pi c^3/L$, where $d$ is the platelet thickness and $L = c/d$ is the aspect ratio. The density $N$ of cracks per unit volume is therefore determined by the volume fraction of platelets $V_f$, i.e. $N = V_f/(\pi c^3/L) = V_f L/\pi c^3$, so that $\rho = 2Nc^3 = 2V_f L/\pi$. Thus for a material in which the platelets grow uniformly at the expense of the matrix material during heat treatment ($L$ constant), the crack density parameter is proportional to the volume fraction $V_f$. For a material in which the platelets grow without increasing the total concentration of platelet phase ($V_f$ constant) [as is the case in some glass-ceramics (Fischer-Cripps and Lawn, 1996)], the crack density parameter depends only on the aspect ratio $L$.

Although we have treated just uniaxial loading, the analysis is readily extendable to more complex, triaxial stress states. It is necessary only to modify the expressions for $\sigma_\beta$ and $\tau_\beta$ in (4) in terms of the orthogonally applied normal stresses. For the special case of superposition of a hydrostatic pressure $p$ onto the uniaxial stress $\sigma$ in Fig. 1, as pertains, for instance, to rock mechanics experiments under confining pressures (Jaeger and Cook, 1971; Paterson, 1978), the normal stress $\sigma_\beta$ increases by $p$ but the shear stress $\tau_\beta$ remains unaltered. Then (10) becomes $\tau_f = \tau_c + \mu p + \mu\sigma \sin^2\beta$, which is equivalent to the same law as before but with an increased cohesion stress $\tau_c + \mu p$. The analysis may also be extended to inhomogeneous fields by using the stress–strain functions derived for uniform stress states in Section 3 as constitutive input into a finite element or other numerical algorithm, as has been done for Hertzian contacts in quasi-plastic ceramics (Fischer-Cripps and Lawn, 1996).

Our analysis has been restricted to non-interacting crack distributions. Strictly, allowance should be made for the fact that the energy $w_i$ of any crack is affected by the presence of the other cracks in the distribution, through both the constitutive relation $\bar{v}(\sigma)$ of (12) and the local stresses experienced by the crack. Various approaches based on "effective medium" or "mean field" approximations have been devised to account for such interactions effects in linear systems (Budiansky and O'Connell, 1976; Horii and Nemat-Nasser, 1983; Aboudi and Benveniste, 1987; Hashin, 1988; Kachanov, 1992). Arguably, additional neighbor–neighbor ("two-body") interaction terms should become manifest in (26) as the separation between adjacent cracks approaches the crack dimension $c$ itself. In the case of penny cracks this condition corresponds approximately to $\rho = 2Nc^3 \approx 2(1/4c^3)c^3 \approx 0.5$. On the other hand, computer simulations for various distributions indicate that elastic moduli for non-interacting, non-overlaping cracks remain accurate to surprisingly high densities, because of a tendency for cancellation of positive and negative interactions. For example, the difference in moduli for two-dimensional random arrays of cracks with and without interactions is $< 5\%$ for densities up to $\rho = 0.7$ (Kachanov, 1992). Accordingly, the present analysis may provide satisfactory approximations for high

densities of cracks. However, if in such systems overlap occurs, interaction effects can no longer be neglected.

The analysis also assumes that frictional sliding occurs at the crack surfaces without any extensile ("wing") cracking at the fault ends. Such extensile cracking has been considered widely in quasi-plastic solids under compression loading, most notably in rocks and concrete (Horii and Nemat-Nasser, 1985; Ashby and Hallam, 1986; Horii and Nemat-Nasser, 1986; Sammis and Ashby, 1986; Nemat-Nasser and Obata, 1988; Kemeny and Cook, 1991; Myer *et al.*, 1992; Nemat-Nasser and Deng, 1994). It has also been demonstrated to occur in some ceramics at Hertzian contacts, e.g. in alumina (Guiberteau *et al.*, 1993; Guiberteau *et al.*, 1994; Wei and Lawn, 1996) and silicon nitride (Xu *et al.*, 1995). In such cases, the fault dimension $c$ increases progressively with loading, and in some cases also with unloading (Padture and Lawn, 1995a, b), further reducing the effective modulus. Where interactions become important, this can lead to strain softening, as reported in the rock and concrete literature (Jaeger and Cook, 1971; Horii and Nemat-Nasser, 1985; Horii and Nemat-Nasser, 1986; Shah *et al.*, 1995).

Finally, some implications concerning fatigue may be noted. We have made an issue of the existence of hysteresis in the loading–unloading–reloading cycles in Fig. 4. The degree of this hysteresis is governed by the friction parameters $\tau_c$ and $\mu$ (as well as the crack configuration parameter $\rho$) in the stress–strain formalism, as demonstrated in Figs 6–8. If these friction parameters are reduced by cyclic attrition at the sliding crack surfaces, the hysteretic loop in Fig. 4 contracts along the stress axis and expands along the strain axis, increasing the system compliance and therefore the degree of quasi-plasticity (Padture and Lawn, 1995b). Any accompanying extensile cracking from the ends of the shear cracks only exacerbates the effect (Lawn *et al.* 1994b). As has been demonstrated in repeat Hertzian contacts in ceramics, the result of such fatigue processes is a progressive damage accumulation that ultimately results in exaggerated strength loss and material removal (Padture and Lawn, 1995a, b).

## ACKNOWLEDGEMENT

This work was funded by the U.S. Air Force Office of Scientific Research.

## REFERENCES

Aboudi, J. and Benvensite, Y. (1987) The effective moduli of cracked bodies in plane deformations. *Engng Fract. Mech.* **26,** 171–184.

An, L., Chan, H. M., Padture, N. P. and Lawn, B. R. (1996) Damage-resistant alumina-based layer composites. *J. Mater. Res.* **11,** 204–210.

Ashby, M. F. and Hallam, S. D. (1986) The failure of brittle solids containing small cracks under compressive stress states. *Acta Metall. Mater.* **34,** 497–510.

Batzle, M. L., Simmons, G. and Siegfried, R. W. (1980) Microcrack closure in rocks under stress: direct observations. *J. Geophys. Res.* **85,** 7072–7090.

Bowden, F. P. and Tabor, D. (1986) *The Friction and Lubrication of Solids*. Clarendon Press, Oxford.

Budiansky, B. and O'Connell, R. J. (1976) Elastic moduli of a cracked solid. *Int. J. Solids Struct.* **12,** 81–97.

Cai, H., Kalceff, M. A. and Lawn, B. R. (1994a) Deformation and fracture of mica-containing glass–ceramics in Hertzian contact. *J. Mater. Res.* **9,** 762–770.

Cai, H., Kalceff, M. A. S., Hooks, B. M., Lawn, B. R. and Chyung, K. (1994b) Cyclic fatigue of a mica-containing glass–ceramic at Hertzian contacts. *J. Mater. Res.* **9,** 2654–2661.

Cox, B. N. and Marshall, D. B. (1991) Stable and unstable solutions for bridged cracks in various specimens. *Acta Metall.* **39,** 579–589.

Evans, A. G. (1990) Perspective on the development of high-toughness ceramics. *J. Am. Ceram. Soc.* **73,** 187–206.

Fischer-Cripps, A. C. and Lawn, B. R. (1996) Indentation stress–strain curves for "quasi-ductile" ceramics. *Acta Mettal.* **44,** 519–527.

Frank, F. C. and Lawn, B. R. (1967) On the theory of Hertzian Fracture. *Proc. R. Soc. Lond.* **A299,** 291–306.

Guiberteau, F., Padture, N. P., Cai, H. and Lawn, B. R. (1993) Indentation fatigue: a simple cyclic Hertzian test for measuring damage accumulation in polycrystalline ceramics. *Phil. Mag.* **A68,** 1003–1016.

Guiberteau, F., Padture, N. P. and Lawn, B. R. (1994) Effect of grain size on Hertzian contact in alumina. *J. Am. Ceram. Soc.* **77,** 1825–1831.

Hashin, Z. (1988) The differential scheme and its application to cracked materials. *J. Mech. Phys. Solids.* **36,** 719–734.

Horii, H. and Nemat-Nasser, S. N. (1983) Overall moduli of solids with microcracks: load-induced anisotropy. *J. Mech. Phys. Solids* **31,** 155–171.

Horii, H. and Nemat-Nasser, S. (1985) Compression-induced microcrack growth in brittle solids: axial splitting and shear failure. *J. Geophys. Res.* **90,** 3105–3125.

Horii, H. and Nemat-Nasser, S. (1986) Brittle failure in compression: splitting, faulting and brittle–ductile transition. *Phil. Trans. R. Soc. Lond.* **319,** 337–374.

Jaeger, J. C. and Cook, N. G. W. (1971) *Fundamentals of Rock Mechanics.* Chapman and Hall, London.

Kachanov, M. (1992) Effective elastic properties of cracked solids: critical review of some basic concepts. *Appl. Mech. Rev.* **45,** 304–335.

Kachanov, M. (1994) Elastic solids with many cracks and related problems. *Adv. Appl. Mech.* **30,** 259–445.

Kemeny, J. M. and Cook, N. G. W. Micromechanics of deformation in rock. In *Toughening Mechanisms in Quasi-Brittle Materials*, ed. S. P. Shah, pp. 287–311. Kluwer Academic Publishers, Dordrecht, The Netherlands.

Kranz, R. L. (1983) Microcracks in rocks: a review. *Tectonophysics* **100,** 449–480.

Lawn, B. R., Padture, N. P., Cai, H. and Guiberteau, F. (1994a), Making ceramics 'ductile'. *Science* **263,** 114–116.

Lawn, B. R., Padture, N. P., Guiberteau, F. and Cai, H. (1994b) A model for microcrack initiation and propagation beneath Hertzian contacts in polycrystaline ceramics. *Acta Mettal.* **42,** 1683–1693.

Mai, Y.-W. and Lawn, B. R. (1987) Crack-interface grain bridging as a fracture resistance mechanism in ceramics: II. Theoretical fracture mechanics model. *J. Am. Ceram. Soc.* **70,** 289–294.

Meredith, P. G., Ayling, M. R., Murrell, S. A. F. and Sammonds, P. R. (1991) Cracking, damage and fracture in stressed rock: a holistic approach. In *Toughening Mechanisms in Quasi-Brittle Materials*, ed. S. P. Shah, pp. 67–89. Kluwer Academic Publishers, Dordrecht, The Netherlands.

Myer, L. R., Kemeny, J. M., Zheng, Z., Suarez, R., Ewy, R. T. and Cook, N. G. W. (1992) Extensile cracking in porous rock under differential compressive stress. *Appl. Mech. Rev.* **45,** 263–280.

Nemat-Nasser, S. and Deng, H. (1994) Strain-rate effect on brittle failure in compression. *Acta Mettal.* **42,** 1013–1024.

Nemat-Nasser, S. and Obata, M. (1988) A microcrack model of dilatancy in brittle materials. *J. Appl. Mech.* **55,** 24–35.

Padture, N. P. and Lawn, B. R. (1994) Toughness properties of silicon carbide with an in-situ-induced heterogeneous grain structure. *J. Am. Ceram. Soc.* **77,** 2518–2522.
Padture, N. P. and Lawn, B. R. (1995a) Contact fatigue of a silicon carbide with a heterogeneous grain structure. *J. Am. Ceram. Soc.* **78,** 1431–1438.
Padture, N. P. and Lawn, B. R. (1995b) Fatigue in ceramics with interconnecting weak interfaces: a study using cyclic Hertzian contacts *Acta Metall.* **43,** 1609–1617.
Paterson, M. S. (1978) *Experimental Rock Deformation—The Brittle Field.* Springer-Verlag, Berlin.
Sammis, C. G. and Ashby, M. F. (1986) The failure of brittle porous solids under compressive stress states. *Acta Metall.* **34,** 511–526.
Shah, S. P., Swartz, S. E. and Ouyang, C. (1995) *Fracture Mechanics of Concrete*: *Applications of Fracture Mechanics to Concrete, Rock, and Other Quasi-Brittle Materials.* John Wiley, New York.
Swanson, P. L., Fairbanks, C. J., Lawn, B. R., Mai, Y.-W. and Hockey, B. J. (1987) Crack-interface grain bridging as a fracture resistance mechanism in ceramics: I. Experimental study on alumina. *J. Am. Ceram. Soc.* **70,** 279–289.
Walsh, J. B. (1965) The effect of cracks on the uniaxial elastic compression of rocks. *J. Geophys. Res.* **70,** 399–411.
Wei, L. and Lawn, B. R. (1996) Thermal wave analysis of contact damage in ceramics: case study on alumina. *J. Mater. Res.* **11,** 939–947.
Wong, T.-F., Szeto, H. and Zhang, J. (1992) Effect of loading path and porosity on the failure mode of porous rocks. *Appl. Mech. Rev.* **45,** 281–293.
Xu, H. H. K., Wei, L., Padture, N. P., Lawn, B. R. and Yeckley, R. L. (1995) Effect of microstructural coarsening on Hertzian contact damage in silicon nitride. *J. Mater. Sci.* **30,** 869–878.
Zhang, J., Wong, T.-F. and Davis, D. M. (1990) Micromechanics of pressure-induced grain crushing in porous rocks. *J. Geophys. Res.* **95,** 341–352.

## APPENDIX A: CRACK ENERGY ANALYSIS FOR STRESS–STRAIN CURVES

In the following derivation the approach used by Budiansky and O'Connell (1976) to calculate stiffness changes in crack systems is generalized to allow for the imposition of nonlinear crack-surface tractions. Figure A1 depicts such a crack system (upper), with constitutive responses (lower), during loading to its final loaded state by two routes. An expression for the stress–strain relation follows by equating the changes in mechanical energy (potential energy of loading system plus strain energy of body) in the two routes.

To start, we restrict our consideration to just normal applied stresses, and leave inclusion of shear stresses until later. Consider first Route 1 in Fig. A1, where the body with nonlinear crack-surface tractions is loaded remotely by the applied stress $\sigma$ (0 to $\sigma_A$), with attendant strain $\varepsilon$ (0 to $\varepsilon_A$). The change in energy from application of the stress from zero to peak is

$$\Delta\phi_a = -V\sigma_A\varepsilon_A + V\int_0^{\varepsilon_A}\sigma\,d\varepsilon$$

$$= -V\int_0^{\sigma_A}\varepsilon\,d\sigma, \tag{A1}$$

where $V$ is the volume of the body.

Now consider Route 2 in Fig. A1, taken in two steps. In the first step, restraining tractions are applied to the crack surfaces to prevent relative displacement of the surfaces as the remote

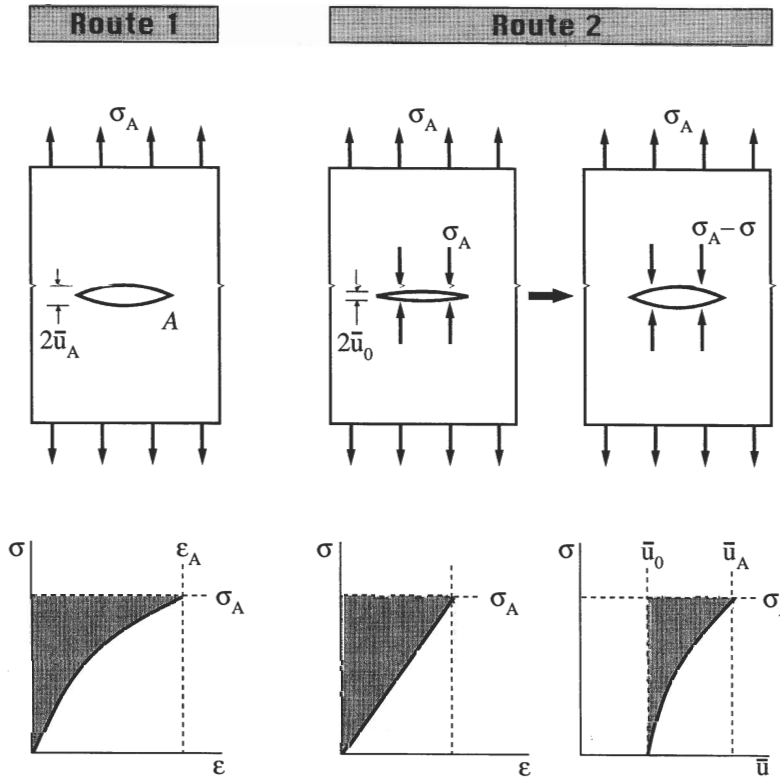


Fig. A1. Equivalent stress states for body containing crack with nonlinear tractions in normal loading. Shaded areas below indicate complementary energies in (A3).

stress $\sigma$ is applied. (In general, the crack faces may be held open in the absence of any applied stress with average separation $2\bar{u}_0$, by residual stresses or wedging displacement.) The response is linear as shown, with change in energy

$$\Delta\phi_b = -V\sigma_A^2/2E_0. \tag{A2}$$

In the second step, the restraining tractions are relaxed by application of opening tractions $\sigma$ on the crack surfaces (0 to $\sigma_A$), allowing the crack opening displacements to increase, thereby releasing energy $w$.

Since the final states in Routes 1 and 2 in Fig. A1 are identical, we may equate the energies $\Delta\phi_a$ and $\Delta\phi_b - w$ (equations A1 and A2):

$$\int_0^{\sigma_A} \varepsilon \, d\sigma = \sigma_A^2/2E_0 + w/V. \tag{A3}$$

The three terms in (A3) correspond to the complementary energies shaded in Fig. A1. Differentiation of (A3) then gives

$$\varepsilon_A = \sigma_A/E_0 + (1/V)\, dw/d\sigma_A. \tag{A4}$$

The energy release $w$ associated with the crack-surface relaxation under the action of the normal applied stress $\sigma$ is expressible in terms of the averaged displacement $\bar{u}$:

$$w = 2A \int_{\bar{u}_0}^{\bar{u}_A} [\sigma_A - \sigma(\bar{u})]\, d\bar{u}$$

$$= 2A \int_0^{\sigma_A} [\bar{u}(\sigma) - \bar{u}_0]\, d\sigma. \tag{A5}$$

(The factor 2 accounts for the definition of $u$ as one half the total crack surface separation.)

If now the crack is inclined at an angle $\beta$ to the applied stress, as in Fig. 1, the relaxation process can be carried out independently for the normal stress component $\sigma_\beta$ and the resolved shear stress component $\tau_\beta$:

$$w = 2A \left[ \int_0^{\sigma_\beta} \Delta\bar{u}(\sigma_\beta)\, d\sigma_\beta + \int_0^{\tau_\beta} \Delta\bar{v}(\tau_\beta)\, d\tau_\beta \right], \tag{A6}$$

with $\Delta\bar{u}(\sigma_\beta) = \bar{u}(\sigma_\beta) - \bar{u}(0)$ and $\Delta\bar{v}(\tau_\beta) = \bar{v}(\tau_\beta) - \bar{v}(0)$ normal and shear displacement changes, respectively.

For a body containing $N$ cracks per unit volume, $w$ in (A4) is replaced by the sum over all cracks contained in volume $V$. The crack energy density is

$$W = (1/V) \sum_{i=1}^{NV} w_i, \tag{A7}$$

and (A4) becomes

$$\varepsilon_A = \sigma_A / E_0 + dW / d\sigma_A. \tag{A8}$$

In the text we drop the subscript A notation in $\sigma$, $\varepsilon$ and $u$, on the understanding there that these quantities denote final states.

## APPENDIX B: CRACK SURFACE DISPLACEMENTS FOR ELLIPTICAL-FRONTED CRACKS

Consider an elliptical crack with semi-axes $c$ and $b$ parallel to the $x$ and $y$ axes in an infinite, homogeneous, isotropic, elastic body. A remotely applied shear stress $\tau = \tau_{xz}$ causes sliding displacements $v_x$. The average displacement $\bar{v}_x$ over the crack plane can be found from a simple extension of an analysis given in Budiansky and O'Connell (1976). They pointed out that the sliding displacement can be written as

$$2v_x(x, y) = B(bc)^{1/2}(1 - x^2/c^2 - y^2/b^2)^{1/2}, \tag{B1}$$

where $B$ is a dimensionless constant (a result that follows directly from Eshelby's discovery that a homogeneous ellipsoidal inclusion under remote loading experiences uniform strain in its interior):

$$B = [4\tau_{xz}(1 - \nu^2)/E_0](b/c)^{1/2}\{k^2/[(k^2 - \nu)E(k) + \nu(1 - k^2)K(k)]\}, \tag{B2}$$

with $E_0$ Young's modulus and $\nu$ Poisson's ratio, $k^2 = (1 - b^2/c^2)$, and $K(k)$ and $E(k)$ complete elliptical integrals of the first and second kind:

$$K(k) = \int_0^{\pi/2} (1 - k^2 \sin^2\theta)^{-1/2}\, d\theta, \tag{B3a}$$

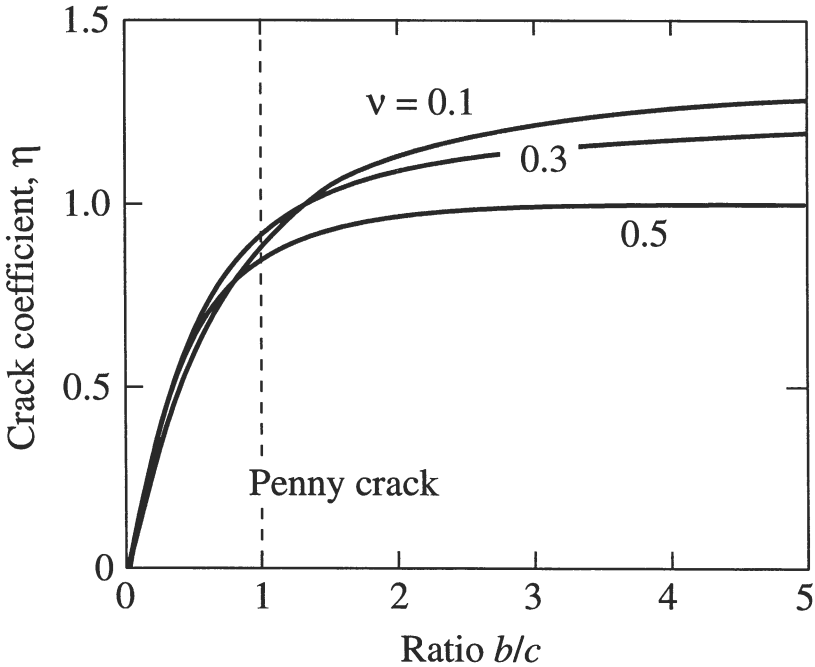


Fig. B1. Plot of elliptical integral function $\eta(b/c)$ for selected values of Poisson's ratio $\nu$.

$$E(k) = \int_0^{\pi/2} (1-k^2 \sin^2 \theta)^{1/2} \, \mathrm{d}\theta. \tag{B3b}$$

The average displacement is obtained by integration of (B1) over the crack area $A = \pi bc$:

$$\begin{aligned} \bar{v}_x &= (1/A)\int v_x(x, y) \, \mathrm{d}A = (B/3)(bc)^{1/2} \\ &= (\eta c/E_0)\tau_{xz}, \end{aligned} \tag{B4}$$

where we define the dimensionless constant $\eta(b/c) = (BE_0/3\tau_{xz})(b/c)^{1/2}$. The function $\eta(b/c)$ is plotted in Fig. B1, for selected values of $\nu$. For a penny crack ($b/c = 1$), $\eta = 8(1+\nu)/3\pi$; for a plane strain crack ($b/c = \infty$), $\eta = 4(1-\nu^2)/3$.

Solutions for a shear stress in an arbitrary direction in the $x$–$y$ plane can be obtained by superposition (with $\tau_{xz}$ obtained by interchanging $c$ and $b$ in the above relations). However, in that case the resultant displacement and the applied shear stress are in different directions, and the formulation requires tensor equivalents.